Bulletin of the Seismological Society of America, Vol. 108, No. 5A, pp. 2580–2593, October 2018, doi: 10.1785/0120180089

Ⓔ

# Earthquake Interaction, Fault Structure, and Source Properties of a Small Sequence in 2017 near Truckee, California

by Rachel L. Hatch, Rachel E. Abercrombie,* Christine J. Ruhl, and Kenneth D. Smith

Abstract We use relocation and source parameter analysis, including stress drop and directivity, to investigate fault structure and earthquake interaction of small-magnitude earthquakes within a sequence in the Walker Lane tectonic region. Two high-angle, left-lateral strike-slip earthquakes ($M_w$ 3.65 foreshock and $M_w$ 3.85 mainshock), occurred 7 min apart, ~20 km north of Truckee, California, on 27 June 2017. Both events were felt over a wide area in northeastern California and northwestern Nevada and happened nearby Holocene fault zones including the Polaris, Mohawk Valley, and Dog Valley Quaternary fault zones that pose a significant hazard to the populated regions in the area. We use waveform cross correlation to relocate the earthquakes and empirical Green's-function methods to estimate the source parameters of all $M_L > 2$ events. Also, we estimate the rupture directivity for the two largest events. We relocate 50 out of 52 earthquakes within the sequence, with an average relative error of < 30 m. The events define a single structure between 5 and 6 km depth, trending ~N45°E and dipping ~70°–80° to the northwest. The distribution of relocations matches the northeast-striking plane from both the moment tensor solutions and computed first-motion focal mechanisms, indicating sinistral strike-slip motion on a previously unmapped fault. We observe average stress drops of ~5 MPa using *P* and *S* waves and spatial variation related to the rupture areas of the foreshock and mainshock. We are able to detect components of directivity toward the northeast for the foreshock ($M_w$ 3.65) and directivity toward the southwest for the mainshock ($M_w$ 3.85), both aligning with the fault plane. This analysis illustrates details in source properties and rupture propagation that can be derived with high-precision event locations within dense regional networks and provides more data and a better understanding as it relates to potential seismic hazard.

*Electronic Supplement:* Figures of waveform fit, relocated earthquakes, example of stress drop, empirical Green's function (EGF), bilateral rupture analysis, tables of stress-drop information, and event IDs.

## Introduction

On 27 June 2017, two $M_w > 3$ earthquakes ($M_w$ 3.65; 09:02:01 UTC, and $M_w$ 3.85; 09:09:21 UTC) occurring ~20 km north of the city of Truckee, California, were felt throughout the Reno–Lake Tahoe region (Fig. 1). These events and subsequent aftershocks occurred in the Walker Lane adjacent to the Sierra Nevada. The well-recorded sequence provides an opportunity to investigate the tectonics and earthquake-source properties of a small earthquake sequence within the seismically active region of the northern Walker Lane.

The 2017 Truckee sequence includes 142 events ($M_L \geq -0.8$, as of 7 October 2017) and is confined to relatively shallow depths (between 5 and 6 km). The sequence behaves as a foreshock–mainshock–aftershock-like sequence, with an unusually large initial foreshock ($M_w$ 3.65) followed immediately by three smaller foreshocks prior to the $M_w$ 3.85 mainshock. About 52 events were detected and located in the first 4 days, including three $M_L > 3$ and eight $M_L > 2$ earthquakes. Activity rates decline to ~1 event/day over the next three months. We confine our detailed analysis of active structures, earthquake stress drops, and source directivity to the initial four-day period of elevated activity. We relocate the earthquakes using a

*Also at Nevada Seismological Laboratory, University of Nevada, Reno, 1664 North Virginia Street, Reno, Nevada 89503.

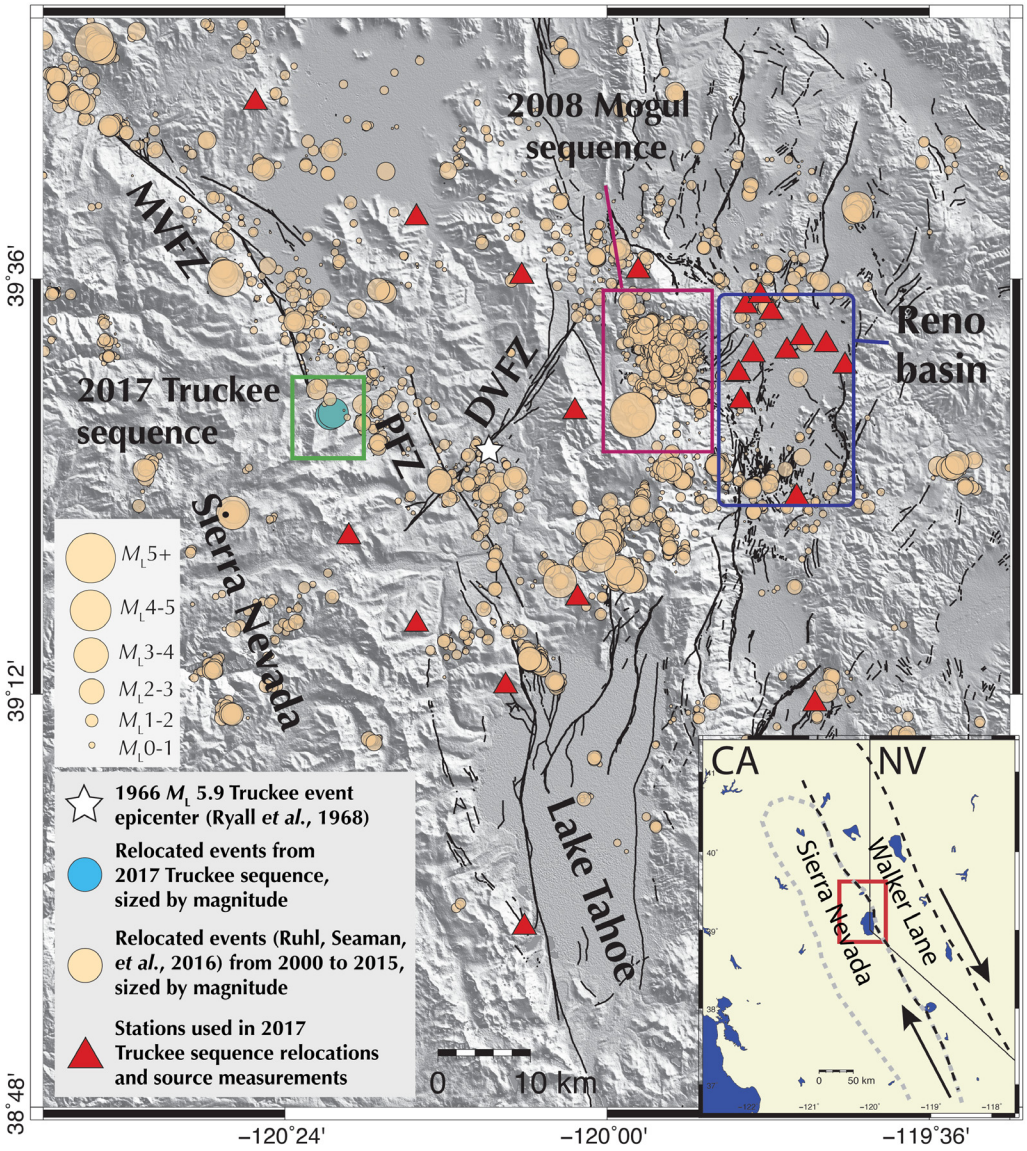


**Figure 1.** Map of northern and western-central Walker Lane region showing relocations of seismicity in the region from 2002 to 2015 (beige filled circles). Green box shows Truckee 2017 sequence; magenta box shows 2008 Mogul sequence (Ruhl *et al.*, 2017); blue box outlines Reno basin; MVFZ, Mohawk Valley fault zone; DVFZ, Dog Valley fault zone; PFZ, Polaris fault zone. (Inset) Map of northern California and western Nevada, including rough outline of the Sierra Nevada Mountains and Walker Lane region; Red box shows area of this figure.

cross-correlation method and then calculate focal mechanisms, stress drop, and rupture directivity. We use these results to identify the sequence structure and its relation to regional tectonics and to investigate source properties and the interactions of the earthquakes within the sequence. The following sections place the 2017 sequence within a local tectonic context and describe past seismicity, as well as previous studies on stress drop and directivity.

## Walker Lane Tectonics and Past Seismicity

The Walker Lane is an ~100-km-wide north-northwest-striking zone of complex and discontinuous strike-slip and normal faulting in the western Basin and Range bordering the Sierra Nevada (Stewart, 1988; Faulds *et al.*, 2008). It extends ~400 km from southeastern California, through western Nevada, and into northern California (Fig. 1). The region accounts for 20%–25% of relative right-lateral motion between the Pacific and North American plates (Argus and Gordon, 1991; Hammond and Thatcher, 2004). South of latitude 39°, dextral shear lies within an ~100-km-wide zone (Oldow *et al.*, 2001). Near latitude 38°, Hammond and Thatcher (2007) find Global Positioning System velocities with respect to stable North America increase east to west across the central Walker Lane, from 6 to 10 mm/yr of dextral shear. North of latitude 39°, the shear zone widens and

splits into a northwest-trending zone of dextral shear and a north-northeast-trending zone of shear and extension (Savage *et al.*, 1995; Svarc *et al.*, 2002; Kreemer and Hammond, 2007). Between latitudes 40° and 41° lies a western zone of ~7 mm/yr dextral shear and an eastern zone of ≤ 3 mm/yr combined dextral shear and extension (Hammond and Thatcher, 2007).

The accommodation of Walker Lane right-lateral shear near the latitude of Lake Tahoe is not well understood (Wesnousky *et al.*, 2012). Possible mechanisms include distributed dextral shear throughout the region on unmapped structures (Bennett *et al.*, 2003), dextral slip focused in the eastern Walker Lane (Hammond and Thatcher, 2004), aseismic slip (Surpless, 2008), block rotations (Wesnousky *et al.*, 2012; Bormann *et al.*, 2016), accommodation on dip-slip structures (Unruh *et al.*, 2003), or a combination thereof. A better understanding of the active structures through seismicity studies will contribute to the understanding of the accommodation of dextral shear within Walker Lane at these latitudes.

Major mapped faults in the Lake Tahoe basin and further north through Truckee are capable of $M_L$ 7 events (Hawkins *et al.*, 1986; Brothers *et al.*, 2009; Hunter *et al.*, 2011). These pose a substantial seismic hazard to populated regions in eastern California and western Nevada. In the area of this study, major faults include (1) the recently discovered dextral Polaris fault (~35 km; slip rate 0.4 mm/yr; Hunter *et al.*, 2011), (2) the identification of the southern extent of the dextral Mohawk Valley fault zone (Gold *et al.*, 2014; geodetic rate 2.9 mm/yr, Hammond *et al.*, 2011; geologic estimate 0.3 mm/yr, Sawyer *et al.*, 2005), and the sinistral Dog Valley fault zone (Hawkins *et al.*, 1986; no known modern slip-rate estimates). The 2017 Truckee sequence occurred at the southern end of the Mohawk Valley fault zone and to the west of the Polaris fault. Although these faults have a potential for large damaging earthquakes, the background seismicity in this area is not often associated with mapped faults.

The northern Walker Lane, north of Lake Tahoe is a persistent source of distributed seismicity, earthquake swarms, and moderate sized ($M_L + 4$) events (Ichinose *et al.*, 2003; Ruhl, Seaman, *et al.*, 2016). Several thousand earthquakes are located annually within the central and northern Walker Lane and along the adjacent Sierra Nevada boundary region (Fig. 1). Event depths include earthquakes as shallow as ~3 km (Ruhl, Abercrombie, *et al.*, 2016) and recent (i.e., 2003 and 2011) dike-injection events as deep as ~30 km (Smith *et al.*, 2016). A seismicity analysis using relocations and a stress inversion of focal mechanisms by Ruhl, Seaman, *et al.* (2016) shows a region of primary strike-slip faulting through the north Truckee area into the northern Walker Lane and a separate region dominated by transtensional deformation directly south of Truckee and north of Lake Tahoe. Based on seismicity studies, this region is interpreted to accommodate the structural transition between normal faulting along the eastern Sierra Nevada block to the south into the dextral faults of the northern Walker Lane.

Despite the predominant right-lateral shear along the Sierra Nevada boundary zone, many moderate events and earthquake swarms often initiate on northeast-striking left-lateral structures (Ichinose *et al.*, 1998; Ruhl, Seaman, *et al.*, 2016). This is true for the largest historical event in the area, the 1966 $M_L$ 5.9 Truckee, California, earthquake (Greensfelder, 1968) and is also the case for many minor alignments of seismicity north of Lake Tahoe (Ruhl, Seaman, *et al.*, 2016). We show that the 2017 Truckee sequence is confined to one of these northeast-striking structures accommodating sinistral motion.

Historically, the specific area of the 2017 Truckee sequence has been seismically active (Ryall *et al.*, 1968; Hawkins *et al.*, 1986), but no documentation of active structures to account for the sequence exists. Significant events identified in the study area include the 1888 $M_L$ 5.9 event at the northern end of the Mohawk Valley fault and the 1966 $M_L$ 5.9 Truckee event that most likely occurred on the Dog Valley fault. Other notable events in the area include the 1914 $M_L$ 6.0 near northeast Reno (Slemmons *et al.*, 1965; Hawkins *et al.*, 1986; dePolo and Garside, 2006), the 1948 $M_L$ 6.0 Verdi, Nevada, earthquake (Slemmons *et al.*, 1965; dePolo *et al.*, 1997), and the 1998 $M_L$ 4.9 Incline Village, Nevada, earthquake (Ichinose *et al.*, 1999). Beneath a suburb of Reno, Nevada, the 2008 Mogul swarm occurred on an unmapped fault, including over 7000 located events (largest event $M_w$ 4.9) within a five-month period (Ruhl, Abercrombie, *et al.*, 2016).

## Earthquake Stress Drop and Directivity

Earthquake stress drops are a measure of the radiated energy from the earthquake source and can be a predictor of high-frequency ground motions. Well-constrained stress-drop estimates from smaller events can be incorporated into seismic hazard assessments, assuming a self-similar scaling relationship (Fry and Gerstenberger, 2011; Holden, 2011), but measurement uncertainties often make it hard to interpret results with confidence (e.g., Abercrombie, 2015, and references therein). Some stress-drop studies show results ranging from higher stress drops for both normal (Shearer *et al.*, 2006) and strike-slip events (Allmann and Shearer, 2009), whereas others report no dependence on focal mechanisms (e.g., Oth, 2013). Some studies suggest that stress drop depends on tectonic setting, depth, or both (e.g., Boyd *et al.*, 2017). The spatial distribution of stress drop can show a systematic pattern of higher and lower stress-drop regions (Goertz-Allmann *et al.*, 2011) that may be related to the local state of stress, loading of nearby fault systems, and the characteristics of fault rupture. A number of studies have attempted to determine whether anthropogenically induced earthquakes have systematically different stress drops than naturally occurring events, with differing results (e.g., Boyd *et al.*, 2017; Huang *et al.*, 2017; Sumy *et al.*, 2017).

Not only can stress drop provide input to seismic hazard estimates, but it can also provide information about local

fault-zone properties and the primary characteristics of an earthquake sequence. Assuming self-similarity, variation in stress drop within a sequence can indicate heterogeneity of fault-zone stress and/or material properties, fault structure interaction (e.g., Madariaga, 1979), and/or the presence of fluids at seismogenic depths. Allmann and Shearer (2007) analyzed the 2004 $M_L$ 6.0 Parkfield earthquake and suggested that rock properties may control stress-drop variation more than absolute stress on the fault. Increased asperity strength due to longer healing periods may also influence sequence evolution. An example being in Sammonds and Ohnaka (1998) who suggested that ruptures on heterogeneous faults with strong asperities are more likely to be obstructed before growing to a large event. Goebel *et al.* (2015) proposed that strong asperities and fault heterogeneity may explain the relatively high stress drops of small- and intermediate-size events they observe. Stress-drop studies have been conducted in the eastern Sierra region. For the $M_L$ 5.8 Round Valley, Nevada, earthquake sequence, Smith and Priestley (1993) observed lower stress drops within the mainshock rupture area. Ruhl *et al.* (2017) also observed an interlocking pattern of high and low stress drops associated with the $M_w$ 4.9 mainshock of the 2008 Mogul sequence; they attribute these observations to fault-zone heterogeneity (i.e., rheology and/or stress).

Additional stress-drop studies occurred nearby. Directly south of the 2017 Truckee sequence, Ichinose *et al.* (1999) also measured stress drop for an $M_L$ 4.9 earthquake near Incline Village, Nevada. They estimated a stress drop of 723 bars (±468 bars). Hawkins *et al.* (1986) used spectral analysis on 17 events near the Dog Valley fault, Truckee, California, with stress drop ranges from 0.005 to 133 bars, with more than 78% below 1 bar (likely underestimated; see Ichinose *et al.*, 1997). Globally, recent efforts to develop meaningful uncertainties in stress-drop estimates have led to more robust results (e.g., Abercrombie, Bannister, *et al.*, 2017; Chen *et al.*, 2017; Huang *et al.*, 2017). Our analysis of the 2017 sequence includes the first modern estimate of earthquake stress drops in the Truckee, California, area.

Rupture directivity effects result in spatial variations in ground-motion amplitude and duration observations and can result in increased shaking in the directivity direction. In relation to seismic hazard assessment, Abrahamson (2000) made the case that to accurately estimate the hazard, directivity should be included as an important source of variability of the long-period ground motion. Considering the geometry of mapped fault systems with respect to the Reno, Truckee, and Lake Tahoe areas (Fig. 1), earthquake directivity effects could contribute to higher ground motions in population centers. In their study of the creeping section on the San Andreas fault, Wang and Rubin (2011) determined a preferred directivity direction toward the southeast, due to a cross-fault material contrast. Although the 2017 Truckee sequence itself did not result in damaging ground motions, documenting directivity contributes important information and observations for future hazard assessments.

Directivity constraints can also assist in identifying the operative fault plane from nodal planes of moment tensors and focal mechanisms. Evidence of directivity can act as an additional confirmation of earthquake relocations, particularly in associating an event with a specific structure in sequences with complex fault geometries.

With advances in instrumentation and analysis, directivity can be constrained in smaller events. Work on directivity of small earthquakes includes Mori (1996), Boatwright (2007), Folesky *et al.* (2016), Abercrombie, Poli, *et al.* (2017), and Prieto *et al.* (2017). In the only estimate of directivity for a moderate event in the north Tahoe/Truckee, California, area, Ichinose *et al.* (1999) constrained rupture directivity for an $M_w$ 4.9 left-lateral strike-slip earthquake in 1988 near Incline Village, Nevada, to the northeast toward Reno.

## Moment Tensor Data and Moment Calculation

We use data from the Nevada Seismological Laboratory (NSL) regional seismic network that includes stations in northeastern California (Fig. 1) to analyze the 2017 Truckee sequence. Data are collected and managed through NSL's regional high-speed microwave network that supports seismic, HD fire camera video, and meteorological data-collection systems (Kent *et al.*, 2015). We use 100 samples/s waveforms from both horizontal and vertical components of broadband, short-period, and strong-motion seismometers for event relocations, stress-drop calculations, and directivity calculations. Moment tensors solutions of the two largest events are determined in routine processing from regional surface waves using the MTINV code of Ichinose *et al.* (2014). Moment tensors are determined interactively by selecting best fits to synthetics of regional long-period (0.01–0.8 Hz) surface waves (Ⓔ Figs. S1 and S2, available in the electronic supplement to this article). Initial automatic moment tensor solutions are reviewed and recomputed prior to posting to the U.S. Geological Survey Comprehensive Catalog. The $M_w$ 3.85 mainshock and $M_w$ 3.65 foreshock show similar strike-slip mechanisms. Computed moments are used for stress-drop calculations for the two larger events.

To calculate small-event moments, we use previous events in the area to develop an $M_L$–$M_0$ relationship. We gather 21 moment tensors from the NSL catalog over the last 15 yrs, including two events from this Truckee sequence, 10 events from the 2008 Mogul sequence (Ruhl, Abercrombie, *et al.*, 2016), and several events from Portola, the city of Tahoe, and elsewhere near Truckee, California, to form the relationship:

$$M_0 = 10^{((M_L \times 1.32)+16.5)}.$$

To account for uncertainty in the $M_0$ estimation, we allow for ±0.3 local magnitude units, representative of the scatter along the linear fit of $M_L$ to $\log(M_0)$.

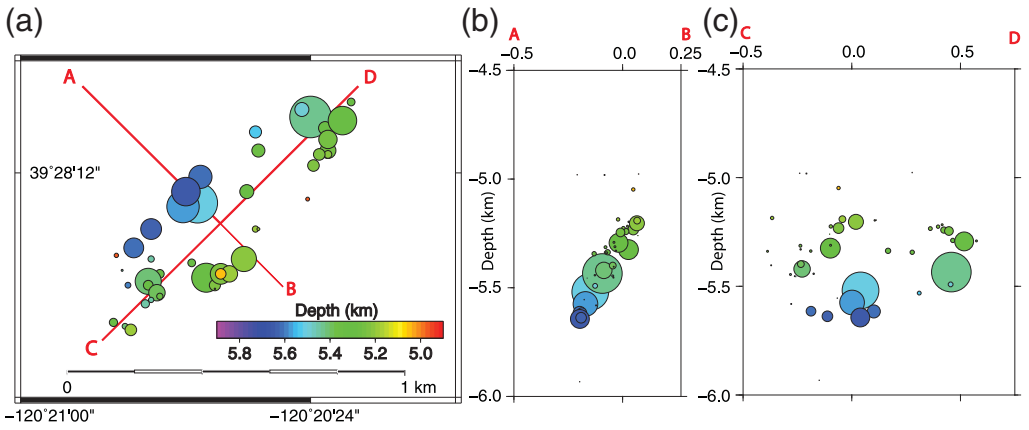


**Figure 2.** (a) Map view of the Truckee 2017 GrowClust relocations, sized by magnitude, colored with depth. (b,c) Cross sections of relocations across line AB and CD, colored with depth.

## Relocation and Focal Mechanisms

To relocate our earthquakes, we apply both absolute and relative relocations using a 1D velocity model, shown in Table 1. We calculate preliminary absolute-event locations using HYPOINVERSE (Klein, 2002) with a datum correction to account for differences in relief (Ruhl, Seaman, *et al.*, 2016). We also include average station travel-time residuals from this initial run as station corrections in a subsequent HYPOINVERSE run to establish a final set of estimated absolute locations. Next, we obtain precise relative relocations by applying the GrowClust algorithm (Trugman and Shearer, 2017). GrowClust uses the 1D velocity model (Table 1) to predict travel times and calculates differential times between earthquakes to relocate them. Using our final set of absolute locations as reference starting locations, GrowClust then applies a hybrid hierarchical clustering algorithm to both group and relocate events within similar event clusters. GrowClust uses the average location of the centroid of the cluster for its reference location. We filter both *P* and *S* waves between 1 and 10 Hz and then cross correlate all events with each other. Cross-correlation values are also used to weight the data by quality and to group events by waveform similarity. Lastly, GrowClust also applies a bootstrap technique to estimate location uncertainties.

Of 52 events within the first 4 days in the sequence, GrowClust successfully relocates 50 ($M_L$ range: −0.8 to 4.1; Fig. 2; updated GrowClust relocations shown in Ⓔ Fig. S3). Two events that did not correlate well enough with the majority of events were not relocated in the GrowClust algorithm. The maximum relative hypocentral location error is 170 m, with an average of less than 30 m (the maximum horizontal error is 21 m and the maximum vertical error is 169 m). The relocations reveal a planar structure, nearly 1-km long, striking ∼N45°E and dipping 70°–80° northwest (Fig. 2); it does not exceed ∼100 m in width. This plane is consistent with the northeast-striking nodal plane being the active fault plane of the two moment tensors. There are no obvious secondary structures in the relocation set; all activity is confined to a single well-defined northeast-striking structure. Relocated events align parallel to the Dog Valley fault but are ∼20 km to the north.

Table 1
1D Velocity Model

| Velocity (km/s) | Depth (km) |
|---|---|
| 5.85 | 0.0 |
| 6.00 | 7.0 |
| 6.70 | 22.1 |
| 7.85 | 28.1 |

The large foreshock ($M_w$ 3.65) is located at the base of and near the central portion of the sequence (Fig. 2). Two smaller foreshocks occur southwest of the initial foreshock at the southwest extent of the sequence. The mainshock ($M_w$ 3.85) is located at the northeast end of the sequence. Aftershocks encircle a region of low seismicity (Fig. 2). The aftershocks of larger earthquakes are typically observed to cluster around the regions of large slip (Woessner *et al.*, 2006); this suggests that the central region of low seismicity may represent an area of higher slip.

We calculate first-motion *P*-wave polarity short-period focal mechanisms for 23 earthquakes using the software application HASH (Hardebeck and Shearer, 2002). We require at least 10 phases for a focal mechanism. The resulting focal mechanisms of the events (Fig. 3) are consistent with the moment tensors and the structure outlined by the relocations, thus confirming left-lateral motion on a steeply dipping northeast-striking fault.

## Source Parameter Calculation

### Spectral Analysis and Earthquake Stress Drop: Methods

We attempt to calculate stress drops ($\Delta\sigma$) for the 11 earthquakes with $M_L \geq 2$, using the Eshelby (1957) relationship:

$$\Delta\sigma = 7/16 \times M_0/r^3,$$

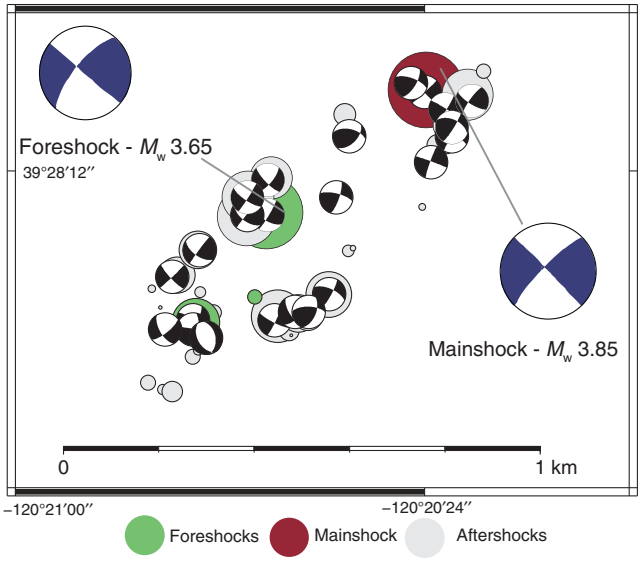


**Figure 3.** Map view with HASH focal mechanisms over relocated events, sized with magnitude, colored by foreshocks (green), mainshock (dark red), and aftershocks (gray); Nevada Seismological Laboratory (NSL) moment tensors shown in blue for the foreshock and mainshock; NSL moment tensor waveform fits and solutions in Ⓔ Figures S1 and S2 (available in the electronic supplement to this article) for foreshock and mainshock.

in which $M_0$ is the moment of the event, in newton·meters, and $r$ is the radius of the seismic rupture, in meters. To measure the source radius, we use the circular source model of Madariaga (1976) and Brune (1970)

$$r = \kappa\beta/f_c,$$

in which we assume $\beta$, the shear-wave velocity, as 3.47 km/s. The constant $\kappa$ depends on whether we use $P$ or $S$ waves and on the choice of source model.

To calculate the corner frequency $f_c$, we use an empirical Green's function (EGF) technique to isolate the source and correct the recorded data for the instrument, path, and site effects. We follow the approach developed by Abercrombie (2014, 2015) and Abercrombie, Bannister, *et al.* (2017) and the approach recently applied to the nearby 2008 Mogul, Nevada, sequence (Fig. 1) by Ruhl *et al.* (2017). The method uses both $P$ and $S$ waves so that they can be used as independent measurements to assess the robustness of the result.

In the method developed by Abercrombie, Bannister, *et al.* (2017), each event of interest (target event) is analyzed separately. For each target earthquake, potential EGFs are all the earthquakes within a specific hypocentral search radius and 1–2.5 M units smaller. For our EGF selection, we estimate the hypocentral search radius for each event by following the Wells and Coppersmith (1994) relationship between magnitude and rupture area but use a minimum value of 500 m to account for location uncertainty. Following Ruhl *et al.* (2017), for each target–EGF waveform pair we select a time window ($t_{\text{window}}$) for both $P$ and $S$ waves, based on the magnitude of the target event and the assumption of constant stress drop:

$$t_{\text{window}} = \text{round}(10 \times M_{\text{L}}^3/15)/10.$$

In the magnitude range used here, this is a close approximation to the *nsec* variable defined by Abercrombie, Bannister, *et al.* (2017), based on the assumption of constant stress drop, but it produces windows that are too short for larger-magnitude events. Next, we calculate the cross correlation between potential EGFs and target events for $P$ and $S$ waves and only preserve EGFs with correlation coefficients of $\geq 0.7$. We use a low-pass filter ($f_{\text{low pass}}$) for both the EGF and target waveforms for the cross correlation only, just below the expected target corner frequency, in order to cross correlate earthquakes of unequal magnitude:

$$f_{\text{low pass}} = 10/t_{\text{window}}.$$

For each target-event seismogram, we calculate the spectra for both $P$ and $S$ waves, the spectral ratio between the target with the EGF, and the source-time functions (STFs) following Prieto *et al.* (2017). For each ratio, we isolate the frequency range in which both target and EGF have a signal-to-noise ratio $\geq 3$, for which we measure noise by attaining the spectra of the seismogram (also time $t_{\text{window}}$) prior to $P$-wave arrival. We stack spectral ratios that successfully pass the criteria of a $< 500$ m hypocentral distance, a magnitude difference between 1 and 2.5 M, a cross correlation of $\geq 0.7$, and a signal-to-noise ratio of $\geq 3$. We also require at least eight target/EGF spectral ratios for each stack. Stacks are calculated by averaging multiple EGF spectral ratios, which is assumed to cancel any azimuthal variation and random noise and boosts the source signal. We bin ratios based on cross-correlation coefficient, and examples of these stacks are shown in Figure 4a,b for the foreshock and mainshock, as well as for a smaller event (Ⓔ Fig. S4). We do not see any systematic dependence of the results on the cross-correlation coefficient (above the minimum of 0.7). We present results obtained using a minimum cross correlation of 0.8 that balances a high cross-correlation coefficient with a sufficient number of EGF ratios. For one event (event ID 593716, $S$ phase), we use a cross-correlation bin of 0.75, due to lack of ratios at higher cross correlations.

Ruhl *et al.* (2017) tested for corner frequencies and finds that the corner frequency is underestimated when it is about two-thirds of the maximum frequency of the spectral ratio. For the Truckee sequence, all corner frequencies measured were within this limit, so it is not likely that our measured corners are being underestimated.

We fit stacked ratios using the Brune (1970) and Boatwright (1980) spectral model and conduct a grid search to find the frequency range in which variance is within 5% of the minimum value to quantify uncertainty (Abercrombie, Bannister, *et al.*, 2017). In common with previous studies (i.e., Abercrombie, Bannister, *et al.*, 2017; Huang *et al.*,

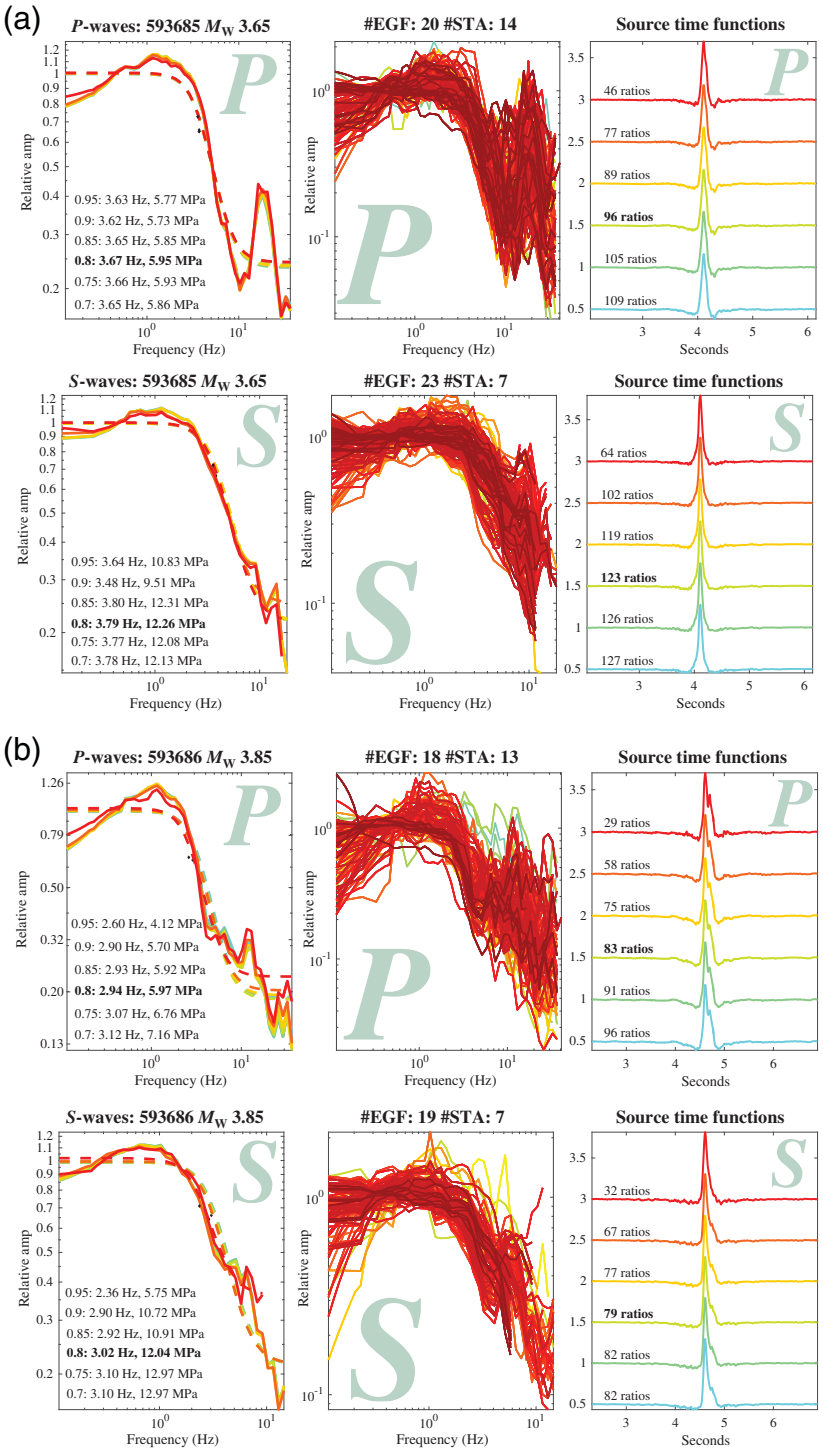


**Figure 4.** (a,b) Stress drop and empirical Green's function (EGF) analysis for both *P* and *S* waves, for the foreshock (event ID 593685) and mainshock (event ID 593686), respectively. From left to right, the first panel shows the fit for the stacked ratios (solid lines) and the fit with the Boatwright (1980) model (dashed lines) in the frequency domain for corresponding cross-correlation bins; cooler colors are lower thresholds (i.e., 0.7), whereas warmer colors are higher thresholds (i.e., 0.95); second panel shows all stacked ratios of all stations used in stacking analysis; third panel shows source time functions (STFs) for different cross-correlation bins, with the number of ratios used in each bin.

2017; Ruhl *et al.*, 2017), we obtain better fits and lower variation between cross-correlation bins when using the Boatwright (1980) model, which has a sharper corner frequency. Variation between cross-correlation bins is within an order of magnitude across all bins, for each target event, adding to the robustness of our results. All results presented here use the Boatwright (1980) model.

We are able to estimate a corner frequency for nine events with sufficient EGFs and frequency bandwidth (see Ⓔ Tables S1 and S2 for detailed results). We adjust our source model and $\kappa$-value based on the ratio of the corner frequency of the *P* wave ($f_{cP}$) and the corner frequency of the *S* wave ($f_{cS}$; Kaneko and Shearer, 2015). Madariaga (1976) calculated $f_{cP}/f_{cS} \sim 1.5$. We find that our ratio $f_{cP}/f_{cS}$ is close to 1, similar to that of Abercrombie, Bannister, *et al.* (2017) and Ruhl *et al.* (2017). Therefore, we follow these studies in using Kaneko and Shearer (2015) circular-source-model values for 0.7 VR (rupture velocity) and use $\kappa$-values of 0.32 and 0.26, thus keeping *P*-value the same as for Madariaga, and change the *S*-value to better reflect our data.

## Spectral Analysis and Earthquake Stress Drop: Results

Results for the nine events are shown in Figure 5. Stress-drop values range from 0.8 to 6.0 MPa (*P*) and 1.3 to 12.3 MPa (*S*) implying that our source model and value of $\kappa$ are not perfect. We obtain average stress drops of 3.3 and 6.7 MPa for *P* and *S* waves, respectively. Spatially, lower stress-drop events outline the rupture zone; the large foreshock and mainshock have the highest stress drop (average *P* and *S* values) of 9.2 MPa (Figs. 4a and 5) and 9.0 MPa (Figs. 4b and 5), respectively. Temporally, large events, occurring early in the sequence, have higher stress drops relative to the aftershocks in the sequence. Eight of the nine events display good fits with the simple circular-rupture model, whereas only the mainshock shows variation in the STF, interpreted as evidence of a more complex rupture (Fig. 4b). We calculate rupture radii of 0.37 km (+0.06/ − 0.04 km) and 0.30 km (+0.04/ − 0.03 km) for the mainshock and foreshock. Errors reflect a 5%

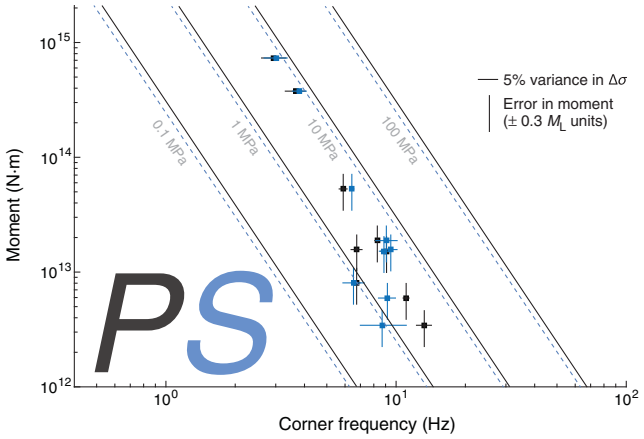


**Figure 5.** Graph showing the corner frequency in Hz versus moment in MPa for *P* (black) and *S* (blue) waves; dark gray lines for *P* (blue dashed lines for *S*) are lines of constant stress drop; horizontal lines indicate a 5% variance in stress drop; vertical error bars show uncertainty in local magnitudes and thus moment calculation ($M_L \pm 0.3$).

variance of the corner frequency pick. When combined, the total area of both ruptures is 0.71 $km^2$ ($+0.23/-0.14$ $km^2$).

The spectra of both the *P* and *S* waves of the two largest events start to decrease below 1 Hz and do not remain flat. This could indicate source complexity (e.g., Uchide and Imanishi, 2016) or be an artifact from our processing or from our data. To ensure our results were not biased or unstable because of this bump, we ran a number of tests; we exclude certain data, increase the minimum signal-to-noise ratio, and remove the lowest frequencies. None of these tests significantly altered our results, indicating that our measurements are relatively robust.

### Rupture Directivity

Abercrombie, Poli, *et al.* (2017) demonstrated that for the best-recorded earthquakes, the STFs from the EGF analysis (Abercrombie, Bannister, *et al.*, 2017) can be stacked by station to reveal azimuthal variation. We follow this approach, based on the stretching method introduced by Warren and Silver (2006) to quantify the azimuthal variation using the whole shape of the STF.

In a unilateral rupture, stations aligned in the rupture direction show narrower pulses, and those in the opposite direction record longer pulses. The stretching method uses the source pulses derived in the EGF method and stretches and compresses the source pulses in the time domain to find the amount of stretching needed to give the highest correlation between pairs of stations. We then perform a grid search to find the rupture velocity, dip, and direction of a line source that best matches the relative variation in observed source duration between stations. This approach removes the uncertainties inherent in subjectively picking start and end times of individual STFs or in modeling spectral parameters. We also test for the possibility of bilateral rupture and an asymmetrical 2:1 rupture.

The best-fitting directivity results for the foreshock and mainshock indicate unilateral rupture in directions consistent with the preferred fault plane from the moment tensors and relocations. The two events rupture in opposite directions (Figs. 6a,b and 7), toward one another. Unilateral directivity results show root mean square values of 0.032 and 0.019 for both the foreshock (Fig. 6a) and the mainshock (Fig. 6b), respectively. The bilateral rupture model fits the data significantly less well and is also inconsistent with slip on the plane indicated by the relocations (Ⓔ Fig. S5a,b). The results from the asymmetrical 2:1 model are identical to those from the unilateral model, indicating that we cannot distinguish asymmetric from purely unilateral rupture (Abercrombie, Poli, *et al.*, 2017; Park and Ishii, 2015). More specifically, our results show directivity toward ~N50°E for the $M_w$ 3.65 foreshock, near the central/southwest end of the fault, and directivity toward ~S40°W for the $M_w$ 3.85 mainshock, at the northeast extent of the sequence, essentially bracketing more than half of the implied ~1 km rupture area (Fig. 7). The dip angle is much less well constrained than the strike, because of the station-earthquake distances, and the rupture velocity is low and poorly constrained. Abercrombie, Poli, *et al.* (2017) find that the fault orientation is well resolved, but the rupture velocity should be considered a minimum, due to the limited bandwidth, consistent with our results.

## Discussion

We use a range of methods to investigate the spatiotemporal evolution of the 2017 Truckee earthquake sequence. The relocations show a planar distribution of events confined to a small area at about 5–6 km depth, trending ~N45°E and dipping to the northwest ~70°–80°. First-motion focal mechanisms as well as NSL calculated moment tensors are consistent with sinistral strike-slip motion on a northwest/southeast-striking plane. We measure stress drops for nine of the largest events in the sequence using a circular-rupture model; the calculated rupture areas for the mainshock and foreshock are shown in map view in Figure 7. We detect directivity in both of the largest events in the sequence; they rupture in opposite directions, toward one another along the fault plane. We discuss hazard and regional tectonic implications and compare stress-drop values, sequence characteristics, and the mainshock and foreshock interaction.

### Regional Tectonic Implications and Hazard

The relocations, focal mechanisms, moment tensors, and directivity all support rupture of a previously unmapped active northeast-striking, left-lateral structure. The Dog Valley fault zone was considerably active from 1920 to 1973 (Hawkins *et al.*, 1986), along with a dense amount of activity to the northwest in this time period, approximately where this current sequence occurred. Refining the location of the Dog

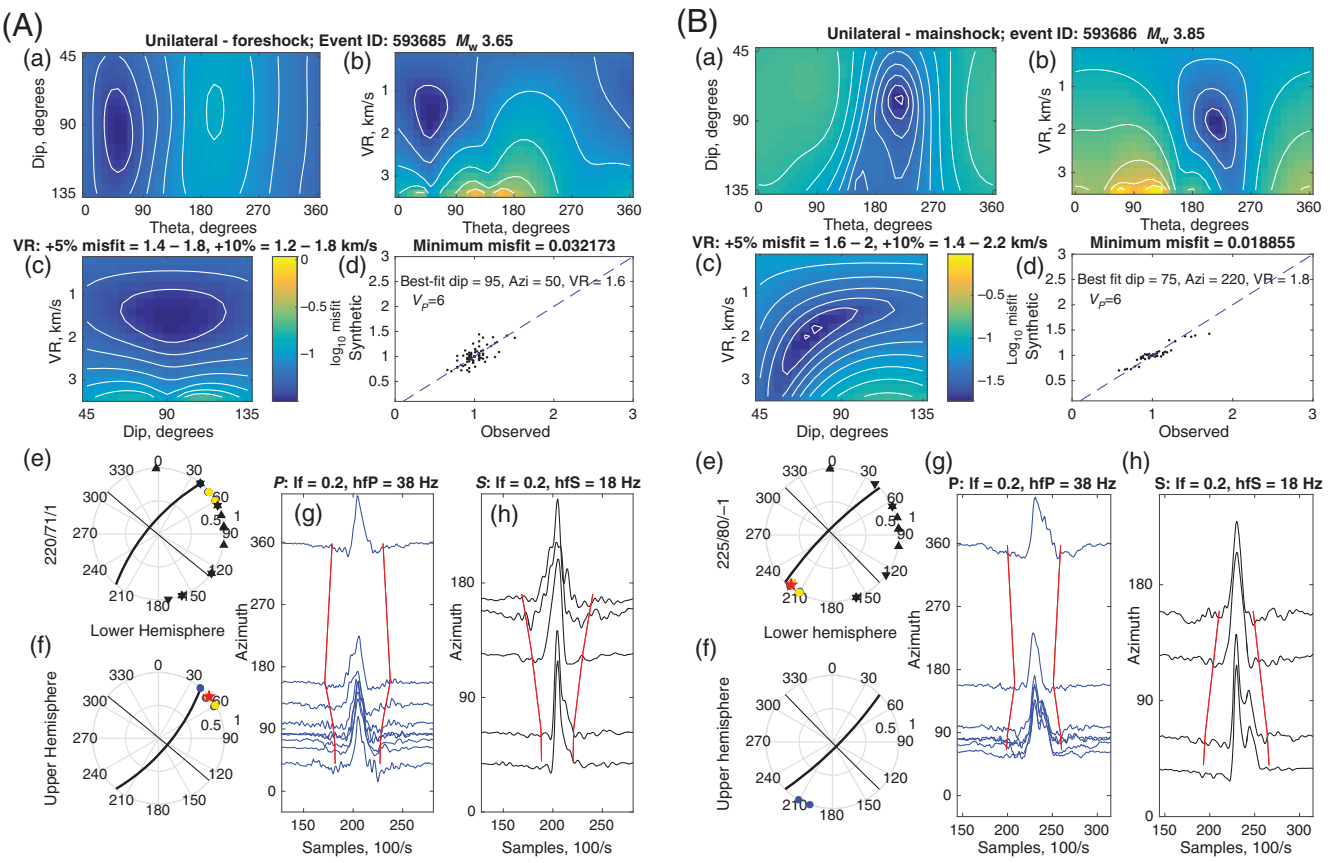


**Figure 6.** Example of unilateral directivity analysis for the (A) foreshock (event ID 593685) and (B) mainshock (event ID 593686), respectively. Top three-color contour graphs (a–c) show misfit between the azimuthal variation in stretching of the STFs and the unilateral line source, as a function of line azimuth (theta), dip (0° = vertically up, 90° = horizontal, and 180° = vertically down), and rupture velocity. (d) The scatter plot shows the relative stretching between each pair of stations from the STFs compared to that predicted by the best-fitting line source; blue dashed line shows 1:1 correspondence. (e) The lower and the (f) upper hemisphere focal spheres; the focal mechanism (strike/dip/rake) is plotted on both (fault-plane thicker line); black triangles are the stations used (upward point for *P*, downward for *S*, and superimposing as a star if both *P* and *S*); the red star is the best-fitting line source (minimum misfit); the yellow region shows the directions with misfit within 5% of the minimum, and blue the directions within 10% of the minimum. (g) *P*-wave (blue) and the (h) *S*-wave (black) STFs used in the analysis; filter frequencies are above the plots. Red lines along plot indicate how the duration varies for the best-fitting line source. They are centered on the STFs and have a mean duration corresponding to the approximate duration of the STF obtained by stacking all stations together. A similar plot showing the best fit with a bilateral model for the foreshock and mainshock is shown in Ⓔ Figure S5a,b. lf, low-frequency limit; hfP, high-frequency *P*-wave limit; hfS, high-frequency *S*-wave limit; $V_P$, *P*-wave velocity (km/s).

Valley fault zone and/or mapping new faults in the area using earthquake relocation may be of interest for future hazard assessment.

Although the fault associated with the 2017 Truckee sequence is not necessarily a large feature, Ruhl, Seaman, *et al.* (2016) pointed out several northeast-trending left-lateral seismicity lineaments in the Reno–Tahoe–Truckee area and measured relocations, the stress field, and focal mechanisms to reveal almost pure strike slip in the region. The Dog Valley fault zone and the fault associated with the Truckee 2017 sequence strike roughly N45°E.

Directivity of a large event (i.e., $M_L \sim 6$, similar to large past events) toward the Reno–Tahoe–Truckee area may increase ground shaking and cause more damage to these areas, due to known and unknown faults. For the 1998 $M_L$ 4.9 earthquake north of Incline Village, Nevada, Ichinose *et al.* (1999) determined rupture to the northeast, toward Reno along a northeast-striking left-lateral strike-slip fault. The Truckee sequence indicated directivity in both directions, toward and away from Reno, so we see no preferred direction in this case. Observations of directivity should continue to be documented to determine if a preferred direction exists in this region. These results may be able to contribute to rupture models and ground-motion prediction in future hazard assessment.

The stress-drop values fall in the normal range from previous studies. We offer these values for future rupture modeling and also aim to gather additional stress-drop values around urban areas in Nevada to isolate possible high stress-drop source zones.

Lastly, left-lateral structures may be accommodating right-lateral slip through simple shear. Wesnousky (2005) adapts the Wilcox *et al.* (1973) study and shows for right-lateral simple shear, conjugate left-lateral (Reidel) shears form at angles nearly perpendicular to the main shear

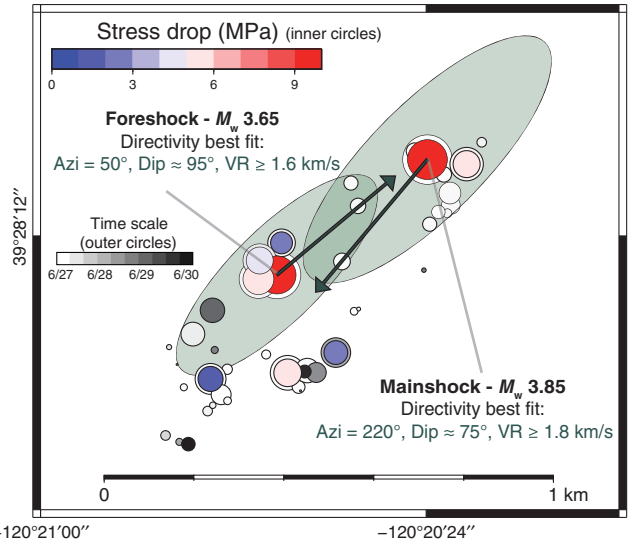


**Figure 7.** Map view of relocated events; inner circles colored by stress drop (MPa) and outer circles colored with time, sized by magnitude; dark teal arrows depict best-fit directions of directivity, and length of arrow represents best-fit rupture velocity. Green ellipses represent projection into map view of simple circular-source model rupture patches of the foreshock ($r = 300$ m) and mainshock ($r = 370$ m) at a 70° dip and trending N45°E; both strike and dip of the projection is approximated from the relocation distribution.

direction, an example being the orientation of the Dog Valley and the Polaris fault zones. It may be necessary to include these northeast-trending fault zones in block models to account for possible bookshelf faulting and rotation of blocks to accommodate right-lateral shear in the northern Walker Lane (Wesnousky *et al.*, 2012; Bormann *et al.*, 2016).

### Stress-Drop Values

Our stress-drop averages match comparatively well, globally and with tectonic environments (Abercrombie, Bannister, *et al.*, 2017). We find most events fit well with the Boatwright (1980) simple circular-source model. When relating to regional averages using a similar method, results match well with the findings from the Ruhl *et al.* (2017) for shallow (2–5 km) earthquakes in the 2008 Mogul sequence (Fig. 1), in which they found averages of ~4.0 MPa for all events studied. The range of values in the Truckee sequence varies over 2 orders of magnitude (0.8–12.3 MPa), which is a smaller range when compared with the Mogul study (0.2–58 MPa) but may simply represent the smaller number of earthquakes included. The comparison with the shallow Mogul earthquakes indicates that stress drop is not dependent on depth in this range.

A number of recent studies have addressed the outstanding question of whether anthropogenically induced earthquakes are different from naturally occurring tectonic events because of different source conditions or the fact that the induced earthquakes tend to be shallower than most tectonic ones. Boyd *et al.* (2017) found that the stress drop of induced earthquakes are not necessarily different than tectonic events at similar depth but that induced earthquakes may be different than tectonic earthquakes because they tend to occur at shallower depths and have a relatively large number of foreshocks. Despite being at similar depths to induced events, there is no evidence that the Truckee sequence was anything but tectonic. This study and the Ruhl *et al.* (2017) study do not find significant differences in stress-drop values with more common deeper-crustal events. For proper comparison of stress drop to induced earthquakes, it is best to compare values using similar methods. However, there is yet to be an induced seismicity sequence analyzed with the method used in the Truckee analysis.

We address possible errors in absolute stress drop from our calculation of moment. Our derived moment equation is constrained by recent local events but could account for notable error in the moment value and therefore for the stress drop for the seven smaller events. We test other moment equations from Abercrombie, Bannister, *et al.* (2017) and Ruhl *et al.* (2017) and find consistency in the relative values of the two largest events and the seven smaller events. Although the absolute values of stress drop may be skewed and lie marginally outside individual value uncertainties, the values do not change drastically (i.e., by a factor of 3) and the spatial variation in relative stress drop (Fig. 7) is likely real. The other tests we carry out, involving different signal-to-noise criteria and excluding particular data types, also reveal that our major findings are robust. These include the narrow stress-drop range, the stress-drop averages, the small spatial variation in stress drop, and that the two largest events have the highest stress drop compared to the smaller, surrounding events.

### Sequence Characteristics: Evolution and Stress-Drop Variation

There is no observed migration of seismicity within the Truckee sequence, indicating an absence of aseismic slip or fluids; the events behave in the manner of a mainshock–aftershock sequences as opposed to swarm-like sequences (Vidale and Shearer, 2006), despite the similarity of magnitude of the foreshock and mainshock. Additionally, there is no evidence to suggest that the Truckee sequence is connected to a water reservoir, large past events, or the deep dike-injection events. Boatwright (2007) showed in a study looking at a small sequence ($M_L$ 3.5–4.1) in California that most of the aftershocks occurred in the direction of rupture, attributed to the unilateral directivity in the events. Event location proximities and unilateral directivity of the main and foreshocks suggests dynamic or static triggering of successive events as the most likely cause.

The stress-drop values along the fault plane show some spatial differences. Comparatively, low stress-drop aftershocks surround the rupture area (Fig. 7). Low stress-drop aftershocks may be attributed to events which rerupture parts of the combined foreshock and mainshock fault plane that

may not have completely healed (e.g., Vidale *et al.*, 1994; Shaw *et al.*, 2015). Given the span of the aftershock zone and our combined rupture areas for the foreshock and mainshock, this would be in line with the aftershocks being in areas that have already ruptured during the foreshock and mainshock events, similar to the Round Valley, Nevada, earthquake sequence (Smith and Priestley, 1993).

Several studies correlate spatial differences of stress drop to rheology on the fault plane. Ruhl *et al.* (2017) observes smaller stress-drop events surrounding a zone of larger stress-drop events in their analysis, attributing the observations to heterogeneous rock properties (i.e., rheology). It is difficult to determine if we are seeing spatial difference in stress drop due to a difference in rheology along the fault, because our values mostly reflect that of previously ruptured areas. However, the interaction of the two largest events shows that rock properties and rheology may play a part in this sequence.

### Mainshock and Foreshock Interaction

Our simple circular-source model shows significant overlap between the rupture areas of the two largest earthquakes (Fig. 7); however, these events may not necessarily be simple sources, because there is directivity in both large events and a more complex STF (Fig. 4b) for the mainshock. Using visual inspection, the sequence zone spans roughly 0.95 km across (±0.1 km) and 0.65 km (±0.05 km) deep, giving a total area of ∼0.62 km$^2$. We interpret the aftershock void in the center of the sequence zone (Fig. 2) as indicative of the combined area of the foreshock and mainshock rupture patches, 0.71 km$^2$ ($+0.23/-0.14$ km$^2$). For the two large events, the combined ruptures would cover the entire aftershock zone.

These observations lead to two questions: (1) did the foreshock and mainshock have overlapping ruptures? (2) What caused the foreshock to stop its rupture and not continue into the mainshock rupture zone? Had the mainshock reruptured a significant portion of the foreshock rupture zone, we would expect to see a smaller stress drop for the mainshock (e.g., Smith and Priestley, 1993). We do see marginally smaller stress-drop values for the mainshock in all tests we conducted, yet they consistently fall within uncertainty limits. While the azimuth of the directivity direction is well constrained, the dip of the rupture direction is not; therefore, it is possible that the foreshock and mainshock rupture zones filled different portions of the rupture plane (i.e., the foreshock on the lower section of the fault plane and the mainshock on the upper section of the fault plane). There is also a lack of aftershocks in between the hypocenters of the large foreshock and mainshock, which we would likely see had there been no overlap of the mainshock and large foreshock rupture areas. This being considered, along with the proximity (< 500 m) of the two large events, we consider the most likely scenario to be that the mainshock had minor overlap with the foreshock.

Now we explore why the foreshock stopped and did not grow into the mainshock rupture zone. Mori (1996) brings up the issue and shows that the Joshua Tree $M_L$ 4.3 foreshock directivity ruptures toward the mainshock hypocenter, similar to the Truckee foreshock. Ideas that control the stopping of the rupture include primary control by material properties of the fault or dynamic properties of the rupture itself (i.e., dynamic friction; Heaton, 1990). Das and Scholz (1981) suggest that foreshocks are small events in the nucleation zone that run into areas of higher strength. In the Truckee sequence, despite unilateral rupture in the direction of the mainshock, the foreshock possibly did not grow into the mainshock rupture patch due to material properties along the fault, as seen elsewhere in the region (e.g., Ruhl *et al.*, 2017). Second, material properties may also explain the higher stress-drop values of both the foreshock and mainshock. In the Goebel *et al.* (2015) study, strong asperities and fault heterogeneity are shown to explain high stress drops of small- and intermediate-size events. Lastly, small asperities on the fault plane can also explain the complexity seen in the STF of the mainshock, shown in Figure 4b (Uchide and Imanishi, 2016). These source observations of the two largest events in the sequence indicate possible fault heterogeneities (i.e., strong asperity) along this structure.

## Conclusions

We relocate 50 events that occurred over a four-day period in the 2017 Truckee, California, sequence, calculate stress drops for nine events, and compute directivity for the two largest events ($M_w$ 3.85 and 3.65).

Relocations show a linear distribution of events confined to a small area at about 5–6 km depth, trending ∼N45°E, and dipping to the northwest ∼70°–80°. This trend matches both the M 3+ moment tensor solution (NSL) focal mechanisms, indicating that the northeast-striking nodal plane is the active fault plane with sinistral strike-slip motion.

We obtain structural information at depth using the relocations and focal mechanism solutions to show that this structure accommodates left-lateral slip. We are able to determine that this sequence did not occur on a currently mapped fault yet took place in the vicinity of the Dog Valley, Polaris, and Mohawk Valley fault zones (Fig. 1).

Our average stress-drop values (∼5 MPa) are within average values when compared with tectonic and induced-earthquake studies and match well with other studies in the area. We observe spatial differences in stress drop and relate them to our foreshock and mainshock rupture areas, where low stress-drop aftershocks likely reruptured within the combined foreshock–mainshock rupture areas. The relatively higher stress drop and the interaction of the two largest events are possibly due to fault heterogeneities (i.e., strong asperity). We detect directivity for the two largest events in the sequence, both rupturing toward each other, in opposite directions.

This analysis illustrates details in source properties and rupture-propagation assessments that can be derived with high-precision event locations. We hope to apply this analysis to more sequences in the area and translate the values to better estimate hazard models.

## Data and Resources

Information on moment tensor solutions were obtained from http://www.seismo.unr.edu/Earthquake (last accessed November 2017). We use the U.S. Geological Survey (USGS) Faults and Folds Database (https://earthquake.usgs.gov/hazards/qfaults/, last accessed October 2015) and the California Geological Survey Fault Activity Map (http://maps.conservation.ca.gov/cgs/fam/, last accessed August 2017) for faults and folds. Map figures were made using the Generic Mapping Tools v. 4.5.14 (www.soest.hawaii.edu/gmt; last accessed November 2015, Wessel and Smith, 1998).

## Acknowledgments

The authors thank the technical staff of the Nevada Seismological Laboratory for their thorough work in picking phase arrivals for the Truckee sequence and maintaining the seismic network, and D. Trugman and P. Shearer for help with the GrowClust analysis. The authors thank three anonymous reviewers for their thoughtful comments, constructive questions, and attention to detail. This work was conducted under U.S. Geological S urvey (USGS) contracts: Great Basin Seismic Network G15AC00052, and National Earthquake Hazards Reduction Program (NEHRP) research Grant G16AP00036, "Analysis of Nevada Seismicity Using Improved Locations, Focal Mechanisms and Stress Drops: Collaborative Research between U.C. San Diego and University of Nevada, Reno."

## References

Abercrombie, R. E. (2014). Stress drops of repeating earthquakes on the San Andreas fault at Parkfield, *Geophys. Res. Lett.* **41,** no. 24, 8784–8791.

Abercrombie, R. E. (2015). Investigating uncertainties in empirical Green's function analysis of earthquake source parameters, *J. Geophys. Res.* **120,** no. 6, 4263–4277.

Abercrombie, R. E., S. C. Bannister, J. Ristau, and D. Doser (2017). Variability of earthquake stress drop in a subduction setting, the Hikurangi Margin, New Zealand, *Geophys. J. Int.* **208,** no. 1, 306–320.

Abercrombie, R. E., P. Poli, and S. Bannister (2017). Earthquake directivity, orientation, and stress drop within the subducting plate at the Hikurangi Margin, New Zealand, *J. Geophys. Res.* **122,** no. 12, 10,176–10,188.

Abrahamson, N. A. (2000). Effects of rupture directivity on probabilistic seismic hazard analysis, *Proc. of the 6th International Conf. on Seismic Zonation*, Vol. 1, Palm Springs, California, 12–15 November 2000, 151–156.

Allmann, B. P., and P. M. Shearer (2007). Spatial and temporal stress drop variations in small earthquakes near Parkfield, California, *J. Geophys. Res.* **112,** no. B4, doi: 10.1029/2006JB004395.

Allmann, B. P., and P. M. Shearer (2009). Global variations of stress drop for moderate to large earthquakes, *J. Geophys. Res.* **114,** no. B1, doi: 10.1029/2008JB005821.

Argus, D. F., and R. G. Gordon (1991). Current Sierra Nevada-North America motion from very long baseline interferometry: Implications for the kinematics of the western United States, *Geology* **19,** no. 11, 1085–1088.

Bennett, R. A., B. P. Wernicke, N. A. Niemi, A. M. Friedrich, and J. L. Davis (2003). Contemporary strain rates in the northern Basin and Range province from GPS data, *Tectonics* **22,** no. 2, doi: 10.1029/2001TC001355.

Boatwright, J. (1980). A spectral theory for circular seismic sources: Simple estimates of source dimension, dynamic stress drop, and radiated seismic energy, *Bull. Seismol. Soc. Am.* **70,** 1–28.

Boatwright, J. (2007). The persistence of directivity in small earthquakes, *Bull. Seismol. Soc. Am.* **97,** no. 6, 1850–1861.

Bormann, J. M., W. C. Hammond, C. Kreemer, and G. Blewitt (2016). Accommodation of missing shear strain in the Central Walker Lane, western North America: Constraints from dense GPS measurements, *Earth Planet. Sci. Lett.* **440,** 169–177.

Boyd, O. S., D. E. McNamara, S. Hartzell, and G. Choy (2017). Influence of lithostatic stress on earthquake stress drops in North America, *Bull. Seismol. Soc. Am.* **107,** no. 2, 856–868.

Brothers, D. S., G. M. Kent, N. W. Driscoll, S. B. Smith, R. Karlin, J. A. Dingler, A. J. Harding, G. G. Seitz, and J. M. Babcock (2009). New constraints on deformation, slip rate, and timing of the most recent earthquake on the west Tahoe–Dollar Point fault, Lake Tahoe basin, California, *Bull. Seismol. Soc. Am.* **99,** no. 2A, 499–519.

Brune, J. N. (1970). Tectonic stress and the spectra of seismic shear waves from earthquakes, *J. Geophys. Res.* **77,** no. 26, 4997–5009.

Chen, X., N. Nakata, C. Pennington, J. Haffener, J. C. Chang, X. He, Z. Zhan, S. Ni, and J. I. Walter (2017). The Pawnee earthquake as a result of the interplay among injection, faults and foreshocks, *Sci. Rep.* **7,** no. 1, 4945, doi: 10.1038/s41598-017-04992-z.

Das, S., and C. H. Scholz (1981). Off-fault aftershock clusters caused by shear stress increase? *Bull. Seismol. Soc. Am.* **71,** no. 5, 1669–1675.

dePolo, C. M., and T. M. Garside (2006). The November 21, 1910 Tonopah Junction earthquake, and the February 18, 1914 and April 24, 1914 Reno earthquakes in Nevada, *Nevada Bureau of Mines and Geology Open-File Rept. 06-2*, 102 pp.

dePolo, C. M., J. G. Anderson, D. M. dePolo, and J. G. Price (1997). Earthquake occurrence in the Reno-Carson City urban corridor, *Seismol. Res. Lett.* **68,** 401–412.

Eshelby, J. D. (1957). The determination of the elastic field of an ellipsoidal inclusion and related problems, *Proc. Math. Phys. Sci.* **241,** 376–396.

Faulds, J. E., C. D. Henry, J. E. Spencer, and S. R. Titley (2008). Tectonic influences on the spatial and temporal evolution of the Walker Lane: An incipient transform fault along the evolving Pacific–North American plate boundary, in *Ores and Orogenesis: Circum-Pacific Tectonics, Geologic Evolution, and Ore Deposits*, Arizona Geological Society Digest 22, 437–470.

Folesky, J., J. Kummerow, S. A. Shapiro, M. Häring, and H. Asanuma (2016). Rupture directivity of fluid-induced microseismic events: Observations from an enhanced geothermal system, *J. Geophys. Res.* **121,** no. 11, 8034–8047.

Fry, B., and M. C. Gerstenberger (2011). Large apparent stresses from the Canterbury earthquakes of 2010 and 2011, *Seismol. Res. Lett.* **82,** no. 6, 833–838.

Goebel, T. H. W., E. Hauksson, P. M. Shearer, and J. P. Ampuero (2015). Stress-drop heterogeneity within tectonically complex regions: A case study of San Gorgonio Pass, southern California, *Geophys. J. Int.* **202,** no. 1, 514–528.

Goertz-Allmann, B. P., A. Goertz, and S. Wiemer (2011). Stress drop variations of induced earthquakes at the Basel geothermal site, *Geophys. Res. Lett.* **38,** no. 9, doi: 10.1029/2011GL047498.

Gold, R. D., R. W. Briggs, F. S. Personius, A. J. Crone, A. M. Shannon, and S. J. Angster (2014). Latest Quaternary paleoseismology and evidence of distributed dextral shear along the Mohawk Valley fault zone, northern Walker Lane, California, *J. Geophys. Res.* **119,** 5014–5032, doi: 10.1002/2014JB010987.

Greensfelder, R. (1968). Aftershocks of the Truckee, California, earthquake of September 12, 1966, *Bull. Seismol. Soc. Am.* **58,** no. 5, 1607–1620.

Hammond, W. C., and W. Thatcher (2004). Contemporary tectonic deformation of the Basin and Range province, western United States: 10 years of observation with the Global Positioning System, *J. Geophys. Res.* **109,** no. B8, doi: 10.1029/2003JB002746.

Hammond, W. C., and W. Thatcher (2007). Crustal deformation across the Sierra Nevada, northern Walker Lane, Basin and Range transition, western United States measured with GPS, 2000–2004, *J. Geophys. Res.* **112,** no. B05411, doi: 10.1029/2006JB004625.

Hammond, W. C., G. Blewitt, and C. Kreemer (2011). Block modeling of crustal deformation of the northern Walker Lane and Basin and Range from GPS velocities, *J. Geophys. Res.* **116,** no. B4, doi: 10.1029/2010JB007817.

Hardebeck, J. L., and P. M. Shearer (2002). A new method for determining first-motion focal mechanisms, *Bull. Seismol. Soc. Am.* **92,** 2264–2276.

Hawkins, F. F., R. LaForge, and R. A. Hansen (1986). Seismotectonic study of the Truckee/Lake Tahoe area, northeastern Sierra Nevada, California for Stampede, Prosser Creek, Boca, and Lake Tahoe dams, *US Bureau of Reclamation 85-4*, Seismotectonic Section, Engineering and Research Center, 210 pp.

Heaton, T. H. (1990). Evidence for and implications of self-healing pulses of slip in earthquake rupture, *Phys. Earth Planet. In.* **64,** no. 1, 1–20.

Holden, C. (2011). Kinematic source model of the 22 February 2011 $M_w$ 6.2 Christchurch earthquake using strong motion data, *Seismol. Res. Lett.* **82,** no. 6, 783–788.

Huang, Y., W. L. Ellsworth, and G. C. Beroza (2017). Stress drops of induced and tectonic earthquakes in the central United States are indistinguishable, *Sci. Adv.* **3,** no. 8, e1700772.

Hunter, L. E., J. F. Howle, R. S. Rose, and G. W. Bawden (2011). LiDAR-assisted identification of an active fault near Truckee, California, *Bull. Seismol. Soc. Am.* **101,** 1162–1181.

Ichinose, G., J. Anderson, K. Smith, D. dePolo, R. Anooshehpoor, R. Schweickert, and M. Lahren (1999). The seismotectonics of the 30 October 1998 Incline Village, Nevada earthquake and its effects, *Seismol. Res. Lett.* **70,** no. 3, 297–305.

Ichinose, G. A., J. G. Anderson, K. D. Smith, and Y. Zeng (2003). Source parameters of eastern California and western Nevada earthquakes from regional moment tensor inversion, *Bull. Seismol. Soc. Am.* **93,** 61–84.

Ichinose, G. A., J. Roman-Nieves, and G. Kraft (2014). Moment tensor inversion toolkit (MTINV) documentation, *Manual and Tutorial, Version 3.0.3*.

Ichinose, G. A., K. D. Smith, and J. G. Anderson (1997). Source parameters of the 15 November 1995 Border Town, Nevada, earthquake sequence, *Bull. Seismol. Soc. Am.* **87,** no. 3, 652–667.

Ichinose, G. A., K. D. Smith, and J. G. Anderson (1998). Moment tensor solutions of the 1994 to 1996 Double Spring Flat, Nevada, earthquake sequence and implications for local tectonic models, *Bull. Seismol. Soc. Am.* **88,** no. 6, 1363–1378.

Kaneko, Y., and P. M. Shearer (2015). Variability of seismic source spectra, estimated stress drop, and radiated energy, derived from cohesive-zone models of symmetrical and asymmetrical circular and elliptical ruptures, *J. Geophys. Res.* **120,** 1053–1079.

Kent, G. M., K. D. Smith, M. C. Williams, D. E. Slater, G. Plank, M. McCarthy, and G. Hidley (2015). A-21st-century-approach to fire-fighting in the western US: How microwave-based seismic networks can change fire suppression from reactive to proactive, *AGU Fall Meeting*, Abstract NH53A–07.

Klein, F. W. (2002). User's guide to HYPOINVERSE-2000, a Fortran program to solve for earthquake locations and magnitudes, *Open-File Rept. 02-171 Version 1.0*.

Kreemer, C., and W. C. Hammond (2007). Geodetic constraints on areal changes in the Pacific–North America plate boundary zone: What controls Basin and Range extension? *Geology* **35,** no. 10, 943–946.

Madariaga, R. (1976). Dynamics of an expanding circular fault, *Bull. Seismol. Soc. Am.* **66,** no. 3, 639–666.

Madariaga, R. (1979). On the relation between seismic moment and stress drop in the presence of stress and strength heterogeneity, *J. Geophys. Res.* **84,** no. B5, doi: 10.1029/JB084iB05p02243.

Mori, J. (1996). Rupture directivity and slip distribution of the M 4.3 foreshock to the 1992 Joshua Tree earthquake, southern California, *Bull. Seismol. Soc. Am.* **86,** no. 3, 805–810.

Oldow, J. S., C. L. V. Aiken, J. L. Hare, J. F. Ferguson, and R. F. Hardyman (2001). Active displacement transfer and differential block motion within the central Walker Lane, western Great Basin, *Geology* **29,** no. 1, 19–22.

Oth, A. (2013). On the characteristics of earthquake stress release variations in Japan, *Earth Planet. Sci. Lett.* **377,** 132–141.

Park, S., and M. Ishii (2015). Inversion for rupture properties based upon 3-D directivity effect and application to deep earthquakes in the Sea of Okhotsk region, *Geophys. J. Int.* **203,** no. 2, 1011–1025.

Prieto, G. A., B. Froment, C. Yu, P. Poli, and R. Abercrombie (2017). Earthquake rupture below the brittle–ductile transition in continental lithospheric mantle, *Sci. Adv.* **3,** no. 3, e1602642.

Ruhl, C. J., R. E. Abercrombie, and K. D. Smith (2017). Spatiotemporal variation of stress drop during the 2008 Mogul, Nevada, earthquake swarm, *J. Geophys. Res.* **122,** no. 10, 8163–8180.

Ruhl, C. J., R. E. Abercrombie, K. D. Smith, and I. Zaliapin (2016). Complex spatiotemporal evolution of the 2008 $M_w$ 4.9 Mogul earthquake swarm (Reno, Nevada): Interplay of fluid and faulting, *J. Geophys. Res.* **121,** no. 11, 8196–8216.

Ruhl, C. J., T. C. Seaman, K. D. Smith, and G. M. Kent (2016). Seismotectonic and seismic hazard implications for the Reno-Tahoe area of the Walker Lane in Nevada and California, in *Applied Geology in California*, AEG Special Volume, 879–895.

Ryall, A., J. D. VanWormer, and A. E. Jones (1968). Triggering of microearthquakes by earth tides, and other features of the Truckee, California, earthquake sequence of September, 1966, *Bull. Seismol. Soc. Am.* **58,** no. 1, 215–248.

Sammonds, P., and M. Ohnaka (1998). Evolution of microseismicity during frictional sliding, *Geophys. Res. Lett.* **25,** no. 5, 699–702.

Savage, J. C., M. Lisowski, J. L. Svarc, and W. K. Gross (1995). Strain accumulation across the central Nevada seismic zone, 1973–1994, *J. Geophys. Res.* **100,** no. B10, 20,257–20,269.

Sawyer, T. L., R. W. Briggs, and A. R. Ramelli (2005). Late Quaternary activity of the southern Mohawk Valley fault zone, northeastern California, *Seismol. Res. Lett.* **76,** no. 2, 248.

Shaw, B. E., K. Richards-Dinger, and J. H. Dieterich (2015). Deterministic model of earthquake clustering shows reduced stress drops for nearby aftershocks, *Geophys. Res. Lett.* **42,** no. 21, 9231–9238.

Shearer, P. M., G. A. Prieto, and E. Hauksson (2006). Comprehensive analysis of earthquake source spectra in southern California, *J. Geophys. Res.* **111,** no. B6, doi: 10.1029/2005JB003979.

Slemmons, D. B., A. E. Jones, and J. I. Gimlett (1965). Catalog of Nevada earthquakes, 1852–1960, *Bull. Seismol. Soc. Am.* **55,** 537–583.

Smith, K. D., and K. F. Priestley (1993). Aftershock stress release along active fault planes of the 1984 Round Valley, California, earthquake sequence applying a time-domain stress drop method, *Bull. Seismol. Soc. Am.* **83,** no. 1, 144–159.

Smith, K. D., G. M. Kent, D. P. Seggern, N. W. Driscoll, and A. Eisses (2016). Evidence for Moho-lower crustal transition depth diking and rifting of the Sierra Nevada microplate, *Geophys. Res. Lett.* **43,** no. 20, doi: 10.1002/2016GL070283.

Stewart, J. H. (1988). Tectonics of the Walker Lane belt, western Great Basin: Mesozoic and Cenozoic deformation in a zone of shear, in *Metamorphism and Crustal Evolution of the Western United States*, W. G. Ernst (Editor), Rubey volume VII, Prentice Hall, Englewood Cliffs, New Jersey, 683–713.

Sumy, D. F., C. J. Neighbors, E. S. Cochran, and K. M. Keranen (2017). Low stress drops observed for aftershocks of the 2011 $M_w$ 5.7 Prague, Oklahoma, earthquake, *J. Geophys. Res.* **122,** 3813–3834, doi: 10.1002/2016JB013153.

Surpless, B. (2008). Modern strain localization in the central Walker Lane, western United States: Implications for the evolution of intraplate deformation in transtensional settings, *Tectonophysics* **457,** nos. 3/4, 239–253.

Svarc, J. L., J. C. Savage, W. H. Prescott, and A. R. Ramelli (2002). Strain accumulation and rotation in western Nevada, 1993–2000, *J. Geophys. Res.* **107,** no. B5, doi: 10.1029/2001JB000579.

Trugman, D. T., and P. M. Shearer (2017). GrowClust: A hierarchical clustering algorithm for relative earthquake relocation, with application to the Spanish Springs and Sheldon, Nevada, earthquake sequences, *Seismol. Res. Lett.* **88,** 379–391.

Uchide, T., and K. Imanishi (2016). Small earthquakes deviate from the omega-square model as revealed by multiple spectral ratio analysis, *Bull. Seismol. Soc. Am.* **106,** no. 3, 1357–1363.

Unruh, J., J. Humphrey, and A. Barron (2003). Transtensional model for the Sierra Nevada frontal fault system, eastern California, *Geology* **31,** no. 4, 327–330.

Vidale, J. E., and P. M. Shearer (2006). A survey of 71 earthquake bursts across southern California: Exploring the role of pore fluid pressure fluctuations and aseismic slip as drivers, *J. Geophys. Res.* **111,** no. B5, doi: 10.1029/2005JB004034.

Vidale, J. E., W. L. Ellsworth, A. Cole, and C. Marone (1994). Variations in rupture process with recurrence interval in a repeated small earthquake, *Nature* **368,** no. 6472, 624.

Wang, E., and A. M. Rubin (2011). Rupture directivity of microearthquakes on the San Andreas fault from spectral ratio inversion, *Geophys. J. Int.* **186,** no. 2, 852–866.

Warren, L. M., and P. G. Silver (2006). Measurement of differential rupture durations as constraints on the source finiteness of deep-focus earthquakes, *J. Geophys. Res.* **111,** no. B6, doi: 10.1029/2005JB004001.

Wells, D. L., and K. J. Coppersmith (1994). New empirical relationships among magnitude, rupture length, rupture width, rupture area, and surface displacement, *Bull. Seismol. Soc. Am.* **84,** no. 4, 974–1002.

Wesnousky, S. G. (2005). Active faulting in the Walker Lane, *Tectonics* **24,** no. TC3009, doi: 10.1029/2004TC001645.

Wesnousky, S. G., J. M. Bormann, C. Kreemer, W. C. Hammond, and J. N. Brune (2012). Neotectonics, geodesy, and seismic hazard in the northern Walker Lane of western North America: Thirty kilometers of crustal shear and no strike-slip? *Earth Planet. Sci. Lett.* **329,** 133–140, doi: 10.1016/j.epsl.2012.02.018.

Wilcox, R. E., T. T. Harding, and D. R. Seely (1973). Basic wrench tectonics, *AAPG Bulletin* **57,** no. 1, 74–96.

Wessel, P., and W. H. F. Smith (1998). New version of the Generic Mapping Tools released, *Eos Trans. AGU* **79,** 579.

Woessner, J., D. Schorlemmer, S. Wiemer, and P. M. Mai (2006). Spatial correlation of aftershock locations and on-fault main shock properties, *J. Geophys. Res.* **111,** no. B8, doi: 10.1029/2005JB003961.

Nevada Seismological Laboratory
University of Nevada, Reno
1664 North Virginia Street
Reno, Nevada 89503
rhatch@nevada.unr.edu
ken@unr.edu
(R.L.H., K.D.S.)

Department of Earth and Environment
Boston University
685 Commonwealth Avenue
Boston, Massachusetts 02215
rea@bu.edu
(R.E.A.)

UC Berkeley Seismological Laboratory
University of California, Berkeley, McCone Hall, 215 Haviland Path #4760
Berkeley, California 94720
cruhl@berkeley.edu
(C.J.R.)

Manuscript received 27 March 2018;
Published Online 14 August 2018